Deciphering the Atomic-Scale Degradation of Carbon-Supported Platinum–Yttrium Nanoalloys during the Oxygen Reduction Reaction in Acidic Medium

Carlos Campos-Roldán, Raphaël Chattot, Jean-Sébastien Filhol, Hazar Guesmi, Nuria Romero, Rémi Bacabe, Pierre-Yves Blanchard, Valentin Vinci, Jakub Drnec, Jacques Rozière, et al.

HAL Id: hal-04672590

https://hal.umontpellier.fr/hal-04672590v1

Submitted on 4 Nov 2024

Deciphering the Atomic-Scale Degradation of Carbon-Supported Platinum-Yttrium Nanoalloys during the Oxygen Reduction Reaction in Acidic Medium

Carlos A. Campos-Roldán†*, Raphaël Chattot†, Jean-Sébastien Filhol†, Hazar Guesmi†, Nuria Romero§, Rémi Bacabe†, Pierre-Yves Blanchard†, Valentin Vinci𝛥, Jakub Drnec𝛥, Jacques Rozière†, Deborah J. Jones†, Sara Cavaliere †*

† ICGM, Univ. Montpellier, CNRS, ENSCM, 34095 Montpellier cedex 5, France

§CNRS, Université de Toulouse, UPS, INPT, Laboratoire de Chimie de Coordination, 205 Route de Narbonne, 31077 Toulouse, France

𝛥 ESRF, European Synchrotron Radiation Facility, 71 Avenue des Martyrs, CS40220, 38043 Grenoble Cedex 9, France

*Corresponding authors:
carlos-augusto.campos-roldan@umontpellier.fr
sara.cavaliere@umontpellier.fr

KEYWORDS:

ABSTRACT

Platinum-yttrium alloys are considered promising candidates to satisfy the challenging requirements for the cathodic oxygen reduction reaction (ORR) in proton exchange membrane fuel cells (PEMFCs). Nevertheless, the practical structure-activity-stability trends of these electrocatalysts in the form of carbon-supported nanostructures are poorly understood, especially under the operating conditions. Herein, carbon-supported Pt_xY nanoalloys were explored during the electrochemical ORR environment, following the atomic-scale degradation steps that the nanoalloys experience during operation. Our results reveal that Pt_xY/C nanoalloys undergo considerable structural modification during the early stage of electrochemical cycling. Moreover, *operando* techniques identify that, during accelerated stress testing under O_2 atmosphere, the majority of nanoalloy degradation occurs during the initial 1,000 electrochemical cycles, and is accompanied by a diminished ORR performance. The observed *operando* structure-activity-stability trends guide further optimization routes for carbon-supported Pt-Y nanoalloys as PEMFC cathode electrocatalysts.

1. INTRODUCTION

Current decarbonization targets are priority in our society, and proton-exchange membrane fuel cells (PEMFCs) have gained attention as energy conversion devices that can contribute importantly to fulfilling these objectives.[1] Nevertheless, their massive production and commercialization are still hindered by technical barriers that need to be overcome, including performance, durability, cost and fuel efficiency,[2, 3] and one particular bottleneck is the electrocatalyst activity and long term durability for the sluggish oxygen reduction reaction (ORR). A well-known approach to enhance the ORR electrocatalytic activity is by alloying Pt with late transition metals (usually Ni, Co, Fe, Cu, *etc*), which also decreases simultaneously the amount of Pt and, therefore, the cost.[4] The long-term stability of Pt-based nanoalloys during the ORR, however, represents a crucial issue that must be tackled.[5-7]

Since their introduction as ORR electrocatalysts in 2009,[8] platinum-yttrium (Pt-Y) alloys have been considered as promising candidates to satisfy the demanding ORR requirements from their predicted high activity and long-term stability. Pioneering theoretical studies[8] concluded that the exceptionally high negative alloy formation energy (-1.02 eV/atom for Pt_3Y)[9] represents a partial thermodynamic barrier for yttrium diffusion through the alloy lattice, which should provide high electrochemical stability. Further research on bulk sputter-cleaned Pt_3Y polycrystalline electrodes[8, 10, 11] and unsupported Pt_xY nanoparticles (NPs)[12] revealed that the high electrocatalytic activity of these alloys stems from the formation of a specific structure, in which the Pt-Y alloy is protected by a thin Pt-rich overlayer, which induces a lateral compressive strain in the Pt-rich shell.[13] Indeed, the surface specific ORR activity showed an exponential dependence on the degree of *ex situ* measured compressive strain of the Pt-rich shell.[12] In the particular case of unsupported Pt_xY NPs, a particle size dependency was also identified, and an

66 outstanding ORR mass activity of 3.05 A mg_{Pt}^{-1} was obtained for NPs of *ca.* 9 nm.[12]

67 Nevertheless, after the applied accelerated stress test (AST), which consisted of 9,000 potential

68 cycles from 0.6 to 1.0 V_{RHE} (triangular potential wave at 100 mV s^{-1}) in O_2-saturated 0.1 M

69 $HClO_4$, the unsupported Pt_xY NPs lost *ca.* 64 % of their initial mass activity.

70 Inspired by the contributions discussed above, further research focused on the challenging

71 production of carbon-supported Pt_xY nanoalloys,[14-17] the practical and desired form for an ORR

72 electrocatalyst. Even though several studies claimed the formation of carbon-supported Pt-Y

73 nanoalloys (more usually yttrium (hydr)oxide-decorated Pt NPs instead of the actual alloy),[18] the

74 first solid evidence was reported in 2016[17] and 2018[15]. However, the measured ORR mass

75 activity of the Pt-Y/C nanoalloys reported so far is in the range between 0.1 and 0.6 A mg_{Pt}^{-1},[14,

76 15, 17, 19-21] which is still far below that of the reference value of 3.05 A mg_{Pt}^{-1} of unsupported 9 nm

77 Pt_xY NPs,[12] *c.f.* **Figure S1** and **Table S1**. This discouraging trend raises critical questions for the

78 viability of Pt_xY/C as ORR electrocatalyst, such as 1) the discrepancy between the theoretically

79 predicted high stability and the experimentally observed high activity loss; 2) the reason for the

80 activity gap between unsupported NPs and carbon-supported NPs; 3) the electrochemical

81 threshold and driving force for alloy degradation under the reaction environment; 4) the

82 electrochemically induced metal dissolution structural transitions during operation, and so on.

83 Of huge potential in this context, the development of *in situ* and *operando* techniques, such as

84 wide-angle synchrotron X-ray scattering (WAXS),[22] X-ray absorption spectroscopy (XAS),[23]

85 *online* inductively coupled plasma mass spectrometry (ICP-MS),[24] *etc.*, has provided

86 fundamental insights at the atomic scale on the degradation of Pt-based electrocatalysts in real or

87 simulated PEMFC electrochemical environments. Nevertheless, the studies that have used these

88 advanced techniques for the characterization of Pt-Y nanoalloys are scarce. For instance,

89 Escudero-Escribano *et al.* have used *in situ* grazing incident X-ray diffraction (GIXRD) to study

90 the formation, induced strain and correlation lengths of the Pt-rich overlayer on Gd/Pt(111)

91 single-crystal electrodes, reporting that the induced compressive strain that the Pt overlayer

92 experiences is relaxed upon repeated electrochemical cycling in the potential range 0.6-1.0 V_{RHE}.

93 This strain relaxion effect is stronger as the upper potential limit increases. To the best of our

94 knowledge, the only publication concerning the *in situ* characterization of Pt-Y nanoalloys is

95 given by Malacrida *et al.*[25] *In situ* ambient pressure X-ray photoelectron spectroscopy (APXPS)

96 was used to investigate the dealloying mechanism of unsupported Pt_xY NPs under near PEMFC

97 operating conditions, when the nature of oxygenated near-surface species was observed as a

98 function of the applied potential.[25] From this study, the authors concluded that a post-synthesis

99 acidic wash is needed to form a protective Pt-rich overlayer, and to avoid the presence/leaching

100 of Y^{3+} cations that may compromise the conduction properties of the PEMFC membrane.

101 Nevertheless, there is still a need for a deeper understanding of the relatively novel Pt_xY/C

102 nanoalloys during the ORR operating conditions.

103 For this purpose, we have synthesized carbon-supported Pt_xY nanoalloys *via* a solid-state

104 approach, and have used advanced techniques for their characterization, *i.e.*, *operando* WAXS,

105 *online* ICP-MS, atomic resolution HAADF-STEM, and have interpreted the results with the

106 assistance of DFT calculations. We have followed, from the early electrochemical activation to

107 the end of the applied AST, the time- and potential-resolved metal dissolution, the variations in

108 crystal structure, the evolution of the local chemical composition and the morphology of Pt_xY/C

109 nanoalloys as ORR electrocatalysts. The extracted results are rationalized and critically

110 discussed, shedding light for the first time on the *operando* relationship between physico-

111 chemical properties, ORR activity and stability of carbon-supported Pt-Y nanoalloys.

112

3. RESULTS AND DISCUSSION

114 Pt_xY/C nanoalloys were synthesized using the carbodiimide complex route developed by Hu *et*

115 *al.*[14] using carbon Ketjenblack EC-300J as a support. The resulting powder was treated *via* an

116 acidic wash in N_2-saturated 0.5 M H_2SO_4[21, 26] (see **Supplementary Information S2**). The as-

117 prepared electrocatalyst crystalline structure, morphology and chemical properties were

118 characterized *ex situ*, and reported in our previous contribution.[21] Briefly, the chemical analysis,

119 determined by ICP-MS, sets a Pt content of *ca.* 27 % *wt.* and an Y content of *ca.* 3 % *wt.* The

120 higher atomic Pt:Y obtained by ICP-MS relative to the Pt_3Y crystalline structure stoichiometry

121 could be related to the formation of the Pt-rich shell and the possible presence of small pure Pt

122 NPs. Besides, the *ex situ* characterization confirms the formation of Pt_3Y nanoalloy, and the

123 presence of a dominant population of NPs of *ca.* 5 nm was observed, as well as some

124 agglomerates of *ca.* 12 nm dispersed over the carbon support.

125 The ORR electrocatalytic activity and long-term stability were investigated using the rotating

126 disk electrode (RDE) technique in 0.1 M $HClO_4$ electrolyte at 25 °C (**Supplementary**

127 **Information S2**). These screenings attest that Pt_xY/C surpasses the initial ORR mass activity of

128 the Pt/C reference (0.58 A mg_{Pt}^{-1} *vs.* 0.23 A mg_{Pt}^{-1} at 0.9 V_{RHE}, respectively). The

129 electrocatalysts' stability was evaluated using an AST inspired from the Fuel Cell Technical

130 Team of the U.S Department of Energy (DoE/FCTT) protocol, which consists of 30,000

131 potential cycles from 0.60 to 0.95 V_{RHE} (square potential wave, 3 s at each potential limit with a

132 transition of 0.5 s in between)[27] in O_2-saturated 0.1 M $HClO_4$. After the AST, the Pt_xY/C and the

133 reference Pt/C lost, respectively, *ca.* 35 % and *ca.* 44 % of their initial mass activity (see **Figure**

134 **S3**). Even though these results clearly show an enhanced performance of Pt_xY/C with respect to

135 the Pt/C reference, the activity value and retention of Pt_xY/C do not correlate with the expected

136 trend.

137 Previously, we have reported that Pt-rare earth nanoalloys undergo significant structure

138 transitions during the early surface conditioning step, namely, the electrochemical activation.[28, 29]

139 Such transitions, often not investigated or underestimated, do induce a considerable effect on the

140 electrocatalyst activity and its retention.[30, 31] Therefore, *online* ICP-MS and *operando* WAXS

141 measurements were conducted to follow any possible degradation of Pt_xY/C during the

142 electrochemical activation, see **Figure 1**.

143
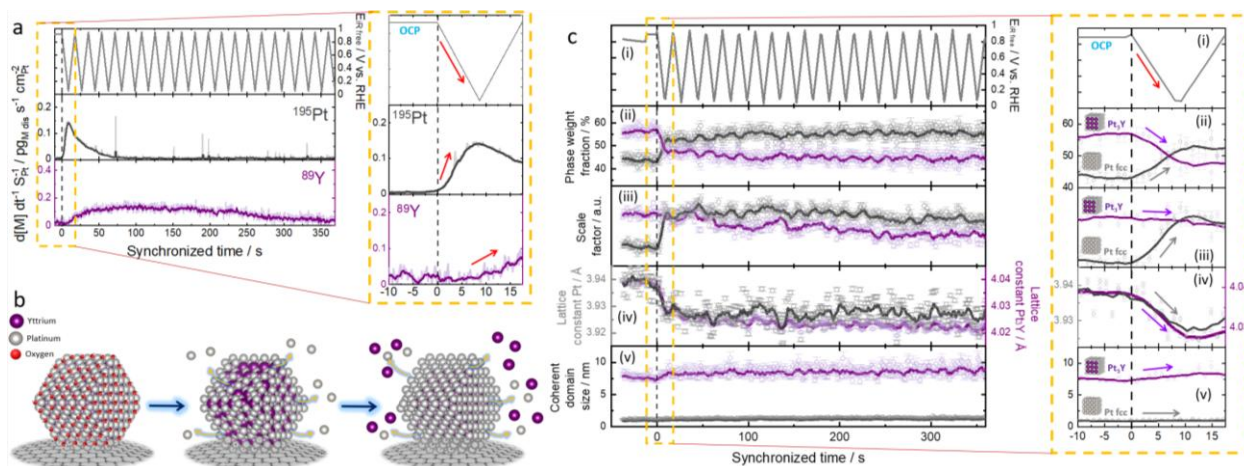
144

145 **Figure 1.** (a) Specific dissolution profiles extracted from *online* ICP-MS measurements; (b)

146 schematic representation of the Pt_xY nanoalloy dissolution and stabilization; and (c)

147 microstructural refined parameters extracted from *operando* WAXS measurements [where (i)

148 indicates the electrode potential wave profile used, (ii) the phase weight fraction, (iii) scale

149 factor, (iv) lattice constant and (v) coherent domain size of the Pt_3Y alloy and Pt phases] of

150 Pt_xY/C during the electrochemical activation. The highlighted region in (a) and (c) indicates the

151 first polarization scan. The arrows serve as a guide to the eye.

152

153 A sharp peak is observed in the specific dissolution profiles, *c.f.* **Figure 1a**, for Pt and a broad

154 peak for Y, which decay through the potential cycling until the signals are stabilized, revealing

155 that the first cathodic scan (first polarization from the open circuit potential, OCP, to 0.05 V_{RHE})

156 induces metal dissolution. It may be noticed that Pt dissolution starts before Y dissolution, which

157 suggests that the partial or the total dissolution of the protective Pt overlayer formed *ex situ* (after

158 the post-synthesis acidic wash) exposes the Y atoms to the acidic electrolyte, see **Figure 1b**.

159 These Y atoms are quickly oxidized into Y^{3+} ($E^0_{Y^{3+}/Y^0}$ = -2.38 V_{SHE}), which represents a strong

160 segregation driving force toward the surface and, eventually, the Y atoms are dissolved. This

161 process might proceed until Pt is sufficiently available to form a thicker protective overlayer,

162 reconstructing the surface and stabilizing the NP structure, see **Figure 1b**. In line with the

163 specific dissolution profiles, the refined parameters extracted from *operando* WAXS

164 measurements, **Figure 1c**, also reveal that as soon as the electrode potential goes from the OCP

165 to 0.05 V_{RHE}, evolution of the structure of the Pt_xY nanoalloys is triggered. Quantitatively, the

166 metallic phase weight fraction of the Pt_3Y alloy decreases from *ca.* 60 % to 45 %, and a Pt face-

167 centered cubic (*fcc*) phase increases from *ca.* 40 % to 55 %. This trend might be linked to the Y

168 dissolution observed in **Figure 1a**. The scale factor intensities, however, seem to be independent

169 from each other, namely, the steady decrease of the Pt_3Y scale factor (related to the Y

170 dissolution) is not correlated to the sudden growth of the *fcc* Pt scale factor. This behavior

171 suggests that the increase of the *fcc* Pt phase might originate from the electrochemical reduction

172 of an amorphous phase containing Pt, even at such low electrode potential.[32] Besides, we do not

173 rule out the probability that the dissolved Pt species might redeposit forming pure Pt crystalline

174 domains during the potential cycling.[33] Furthermore, during the electrochemical activation, the

8

175   lattice constant of both Pt$_3$Y and *fcc* Pt phases experienced a contraction of *ca.* -0.4 % and -0.5

176   %, respectively. Finally, while the average coherent domain size of the Pt$_3$Y phase slightly grows

177   from *ca.* 7.5 nm to 8 nm, that of the *fcc* Pt phase seems to be almost constant (*ca.* 1.2 nm).

178   After the electrochemical activation, three potentiodynamic cycles at 5 mV s^{-1}, from 0.05 to 0.95

179   V$_{RHE}$, were performed to clearly resolve the transient dissolution behavior of Pt and Y. **Figure**

180   **2a** shows the specific dissolution profiles of Pt$_x$Y/C under these conditions. In agreement with

181   the literature,[24, 33-37] the predominant Pt dissolution signal is located at the cathodic scan. This

182   feature is related to the electrochemical reduction of the formed Pt oxides.[35] Besides, the specific

183   Pt dissolution profile also reveals the presence of an additional anodic dissolution peak during

184   the first potential cycle. This signal could be associated with the dissolution of low-coordinated

185   sites through the surface oxidation.[24] Moreover, the Y dissolution follows the first anodic Pt

186   dissolution, and low-intense broad signals appear during the cathodic Pt dissolution, suggesting

187   the stabilization of a protective Pt-rich shell after the electrochemical activation.

188

189
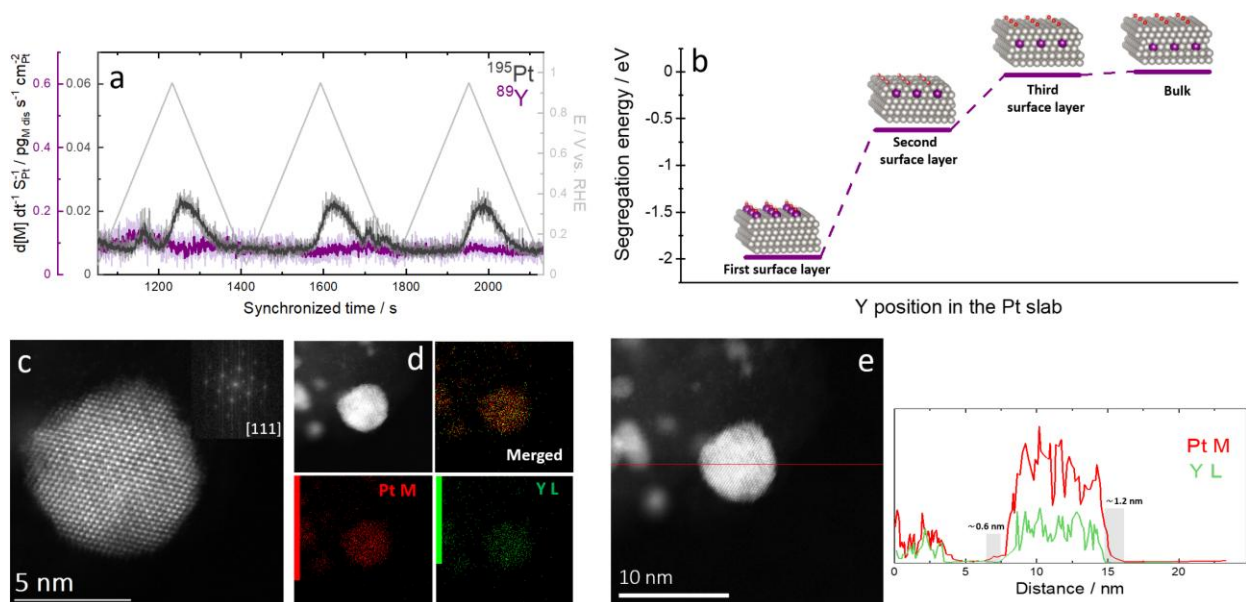
Figure 2. (a) Specific dissolution profiles of Pt_xY/C acquired during slow potentiodynamic cycles (3 cycles at 5 mV s^{-1}); (b) OH-adsorption induced segregation energy as function of the Y position in the Pt slab. The negative values of segregation energies indicate the preference of Y to migrate toward the surface. Representative HAADF-STEM analysis after the electrochemical activation of Pt_xY/C: (c) atomic resolution micrograph (the insert shows the corresponding SAED); (d) EDX elemental mapping; and (e) EDX line scan chemical analysis.

For the sake of clarity, **Figure 2b** exhibits the OH-adsorption induced segregation energy diagram as function of the Y atom position in the Pt slab, *i.e.,* Y atoms exposed at the surface (first surface layer) and protected by *n* Pt monolayers (*n* =1, 2 or 3). This diagram unveils that Y atoms present a strong affinity for OH, which favors their segregation towards the surface and eventually their dissolution (the more negative the segregation energy, the easier the segregation), in line with previous reports on Pt_3Y alloys covered by a Pt monolayer.[38] Notwithstanding, this trend is suppressed once Y atoms are protected by at least 3 Pt monolayers, stabilizing a core/shell (Pt-Y alloy/Pt-rich overlayer) structure. To gain more insights, high resolution HAADF-STEM analyses were carried out after the electrochemical activation, and are presented in **Figure 2c-e** and **Supplementary Information S3**. The average particle size measured *ex situ* is not affected by the electrochemical activation (see below). Besides, the atomic-resolution micrographs and their respective EDX chemical mapping/profiles clearly confirm the presence of the Pt-Y nanoalloy after the electrochemical activation, as NPs presenting a Pt enrichment of 0.6-1.2 nm at the surface. Considering that the thickness of an atomic monolayer of Pt is ~ 0.2 nm,[39] the observed Pt-rich overlayer is 3-6 atom thick, in agreement with the diagram shown in **Figure 2b**.

213   Following the Pt_xY/C nanoalloy stabilization after electrochemical activation, the effect of the

214   square potential wave used in the AST on compositional degradation was investigated by

215   electrochemical *online* ICP-MS. To clearly deconvolute and resolve the dissolution events during

216   the square potential wave, we have held the lower and upper potential limits (0.60 and 0.95 V_{RHE}

217   respectively) for 3 min, following a slow transition between them at 5 mV s^{-1}. **Figure 3a** shows

218   the acquired specific dissolution profiles using three cycles under the aforementioned conditions.

219   Looking at the Pt specific dissolution profile, the anodic dissolution signal through the surface

220   oxidation (yellow arrows in **Figure 3a-b**) peaks as soon as the electrode potential reaches 0.95

221   V_{RHE}, followed by a slow decay. This anodic dissolution event could be associated with the

222   formation and dissolution of metastable Pt species (*e.g.*, amorphous surface oxides,[40] $Pt-O_xH_y$[41]),

223   the origin of which comes from the slow Pt oxidation kinetics.[40] After the formation of a stable

224   Pt oxide, signal decay is observed indicating that the surface is passivated. Meanwhile, the

225   cathodic dissolution event through the reduction of the stabilized Pt oxides (red arrows in **Figure**

226   **3a-b**) takes place, and results in a more intense single peak. This signal has been largely

227   attributed to the oxide place-exchange mechanism, *i.e.*, the exchange of the original lattice sites

228   of surface Pt atoms by O atoms. Simultaneously, the Y specific dissolution profile presents

229   signals during the first cycle at both anodic and cathodic regimes, which are attenuated during

230   the second and third cycles. Based on **Figure 2b,** it might be expected that once the stabilized Pt

231   shell is partially dissolved, its thickness eventually decreases, leading to higher segregation

232   driving force of the previously protected Y atoms, and to the subsequent dissolution of Y until Pt

233   diffusion re-stabilizes the NP structure. This observation might suggest that the stabilization of

234   the Pt-rich shell is critical in hampering Pt-Y segregation.

235
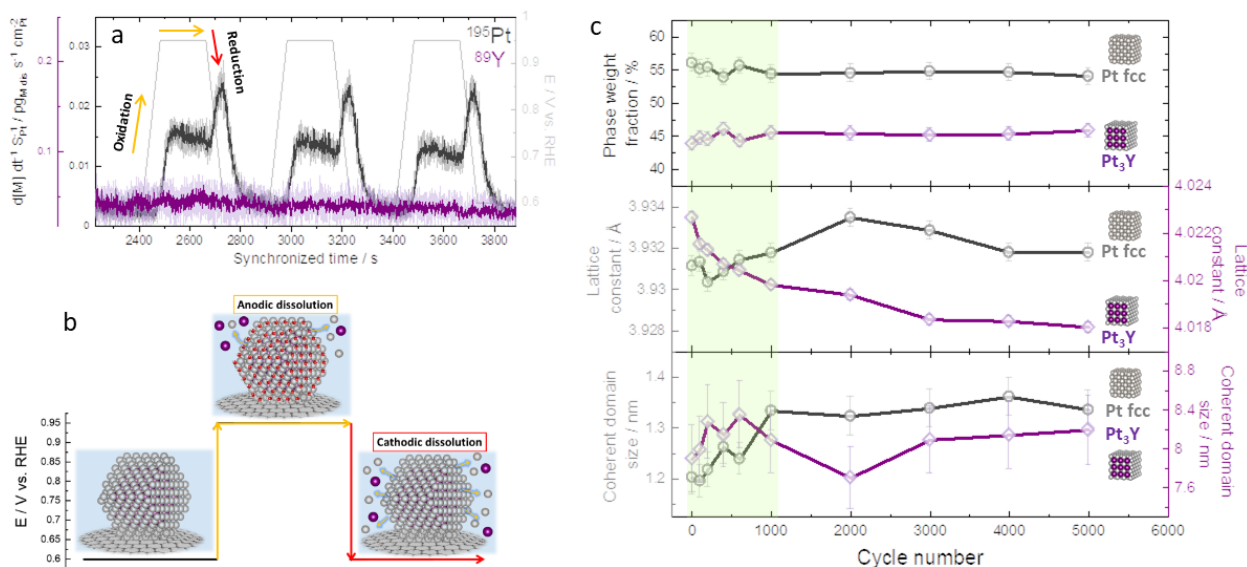
Figure 3. (a) Specific dissolution profiles of Pt_xY/C acquired during simulated AST potential cycles (square-like wave, $0.60 - 0.95$ V_{RHE}, 3 min at each potential limit with a transition between them at 5 mV s^{-1}). The yellow and red arrows (oxidation and reduction, respectively) serve as a guide to the eye. (b) schematic representation of the Pt_xY/C dissolution during the AST potential cycles; (c) microstructural refined parameters extracted from *operando* WAXS measurements (metallic weight phase fraction, lattice constant and coherent domain size) of the Pt_3Y alloy and Pt phases detected during the applied AST (square-like wave, $0.60 - 0.95$ V_{RHE}, 3 s at each potential limit with a transition between them of 0.5 s).

Furthermore, the degradation of the Pt_xY/C nanoalloys during the AST (square potential wave, 3 s at each potential limit with a transition of 0.5 s between) was followed by means of *operando* WAXS and *online* ICP-MS in O_2-saturated 0.1 M $HClO_4$ at 25 °C. The evolution of the WAXS refined microstructural parameters during the AST (5,000 cycles) are shown in **Figure 3c.** The metal phase weight fraction of the Pt_3Y alloy lies between 43 - 48 % during the first 1,000 cycles, and reaches an almost constant value of *ca.* 45 % afterwards. Moreover, during the first 1,000 cycles, the metal phase weight fraction of the *fcc* Pt phase fluctuates between 57 - 52 %, and stabilizes *ca.* 55 % afterwards. While the lattice constant of the *fcc* Pt phases underwent an

12

254   increasing trend (lattice constant expansion), the Pt_3Y phase follows a decreasing behavior

255   (lattice constant contraction). This trend clearly reflects the expected steady loss of the

256   compressive strain effect, with negative effect on the electrocatalytic ORR performance. Finally,

257   the average coherent domain size trend of the Pt_3Y phase revealed a slight increase from *ca.* 7.8

258   nm to 8.4 nm during the first 600 cycles, continuing to *ca.* 8 nm (1,000 cycles), *ca.*7.7 nm (2,000

259   cycles) and *ca.* 8 nm thereafter. Besides, the *fcc* Pt phase slight grew during the first 1,000 cycles

260   from *ca.* 1.20 nm to 1.35 nm, achieving an almost constant value of *ca.* 1.37 nm thenceforth.

261   Therefore, the strongest structural degradation during the AST takes place during the first 1000

262   cycles, in line with previous results on Gd/Pt(111) single-crystal electrodes.

263   Owing to the fact that the most pronounced microstructural variations are discernible during the

264   first 1,000 cycles, the Pt and Y dissolution were monitored by *online* ICP-MS during the first

265   1,000 cycles of the AST (**Supplementary Information S4**). The total dissolved Pt and Y under

266   these conditions, *i.e.*, the integrated specific dissolution rates, are *ca.* 155 pg and 201 pg,

267   respectively, which represent a loss of 0.01 % and 0.13 % of the initial electrode loading after

268   1,000 AST cycles.

269   Enhanced kinetics of the sluggish ORR in acidic medium require the binding energies (ΔE) of

270   the key reaction intermediates, *i.e*., O* and OH*, to be weaker than those with Pt (111) by ~0.2

271   eV and ~0.1 eV, respectively.[42] DFT computations were performed to track the ΔE_{O*} and ΔE_{OH*}

272   as a function of the Pt-Pt interatomic distance, *c.f.* **Figure 4 and Supplementary Information**

273   **S5**. The Pt-Pt interatomic distances of Pt_xY/C nanoalloys during the AST were extracted from

274   the *operando* WAXS measurements and are plotted in **Figure 4**, from which a modest

275   weakening of ΔE_{O*} (~ 0.02 eV) and ΔE_{OH*} (~ 0.001 eV) respect to Pt (111) may be observed.

276 This result indicates that the induced compressive strain is attenuated by the thickening of the Pt

277 overlayer, which leads to lower ORR activity.
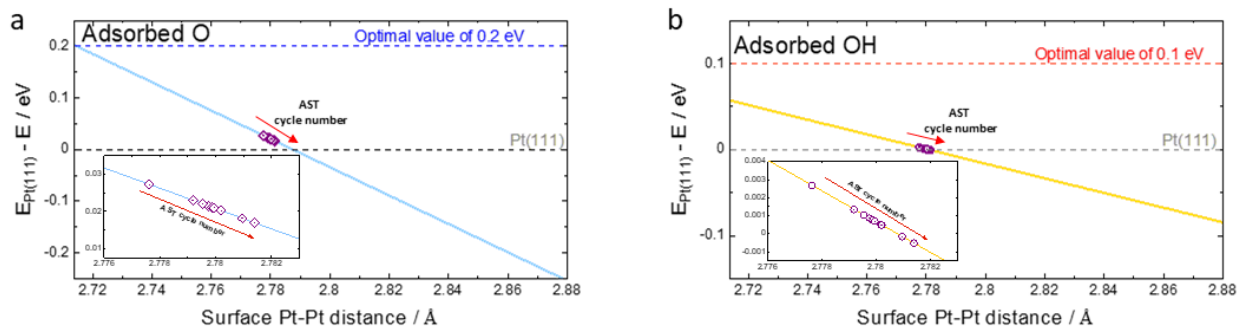
278

279 **Figure 4.** DFT calculated binding energies, with respect to Pt (111) surface, of (a) adsorbed O,

280 and (b) adsorbed OH as function of the Pt-Pt interatomic distance. Purple points represent the

281 experimental average Pt-Pt interatomic distance of Pt_xY/C nanoalloys during the AST (5000

282 square-like wave, $0.60 - 0.95$ V_{RHE}, 3 s at each potential limit with a transition between them of

283 0.5 s).

284

285 With this knowledge, the local morphology and chemical composition of the Pt_xY/C

286 electrocatalyst were investigated after the AST in the RDE setup (30,000 square potential wave,

287 3 s at each potential limit with a transition of 0.5 s between in O_2-saturated 0.1 M $HClO_4$ at 25

288 °C) using high resolution HAADF-STEM analyses, *c.f.* **Figure 5** and **Supplementary**

289 **Information S6**. **Figure 5a** shows the evolution of the average particle size from the *ex situ* state

290 to the end of the AST: while the electrochemical activation does not strongly affect the average

291 particle size, the potential cycling of the AST causes a growth of the electrocatalyst particles

292 from 5.4 nm to 6.6 nm, in line with the average coherent domain size trend in **Figure 3c**. The

293 ECSA variations shown in **Figure S3** might be related to this particle size evolution. Although

294 the acquired micrographs indicate the predominance of dense NPs, the presence of porous

295   structures after the AST was also observed (**Supplementary Information S6**), which are

296   expected due to the dealloying process occurring on potential cycling.[7, 39] The atomic-resolution

297   micrographs and their respective EDX chemical mapping/profiles, **Figure 5b-d,** clearly confirm

298   the presence of the Pt-Y nanoalloy after the AST, with a thicker Pt enrichment at the border of

299   the NPs of *ca.* 1.2-1.6 nm, being equivalent to a Pt shell of 6-8 atom thick.

300
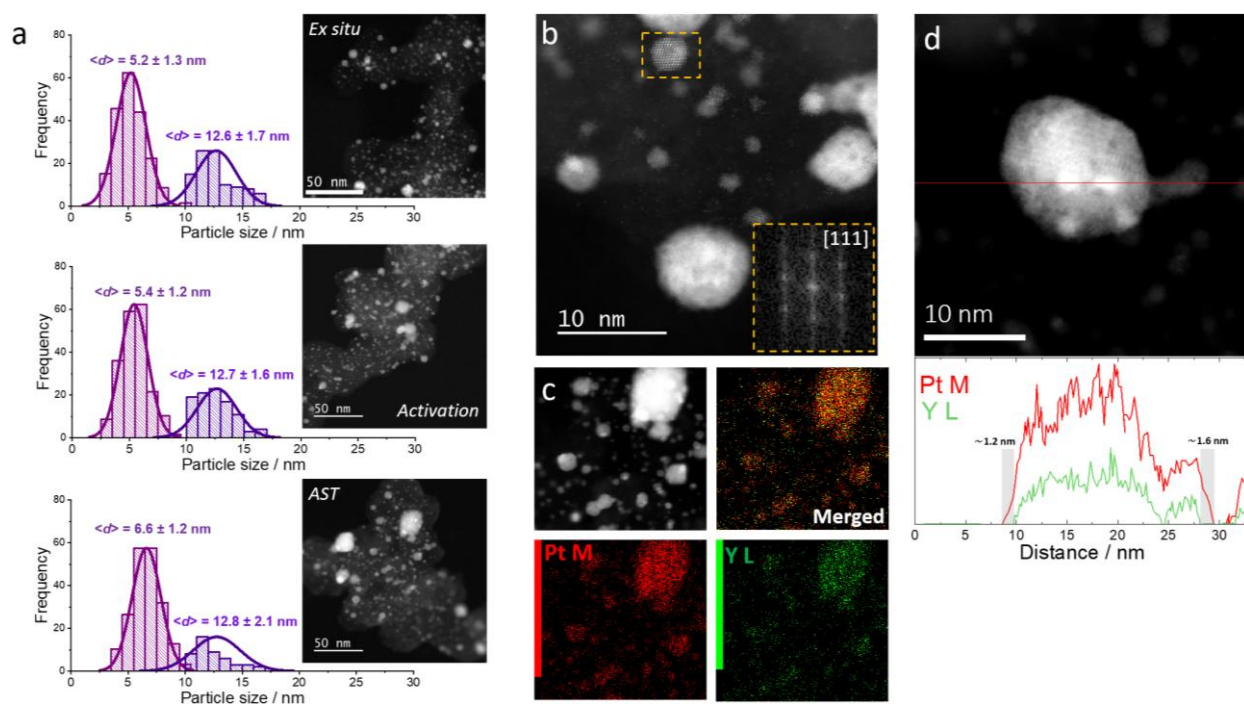
302 **Figure 5.** Representative HAADF-STEM analysis of Pt_xY/C after the AST: (a) evolution of the

303 average particle size, from the *ex situ* state, the electrochemical activation and at the end of the

304 AST; (b) atomic resolution micrograph (the insert shows the corresponding SAED); (c) EDX

305 elemental mapping; and (d) EDX line scan chemical analysis.

306

307 **4. CONCLUSION**

15

308 Carbon-supported Pt_xY nanoalloys were extensively studied, for the first time, under the

309 electrochemical conditions for the ORR by means of *operando* WAXS, *online* ICP-MS, atomic

310 resolution HAADF-STEM and DFT calculations. This allowed monitoring of the atomic-scale

311 degradation steps undergone by the electrocatalyst from the early electrode surface conditioning

312 (or electrochemical activation) to the end of the applied AST. Such results clearly revealed that

313 the Pt_xY/C nanoalloys underwent considerable degradation during the early operation steps

314 (electrochemical activation), with metal dissolution and crystalline structure evolution being

315 observed, and surface reconstruction.

316 Furthermore, *operando* measurements identified that the strongest nanoalloy degradation, in

317 terms of metal dissolution and structural evolution, takes place during the first AST 1,000 cycles

318 under O_2 atmosphere, which eventually diminished the ORR kinetic benefit from the Pt-Y alloy.

319 Although the expected high ORR performance of Pt_xY/C was not observed, the proposed

320 *operando* structure-activity-stability trends guides further optimization of the delicate

321 activity/stability trade-off of this system. Besides, we believe that this work might inspire further

322 in-depth understanding of the degradation of carbon-supported Pt-based nanoalloys during the

323 harsh ORR electrochemical environment.

324

325 **AUTHOR INFORMATION**

326 **Corresponding Authors**

327 **Carlos A. Campos-Roldán*

328 *Email:* carlos-augusto.campos-roldan@umontpellier.fr

329   *Sara Cavaliere

330   *Email:* sara.cavaliere@umontpellier.fr

331

332   **ORCID**

333   C.A. Campos-Roldán: 0000-0002-1517-9037

334   R. Chattot: 0000-0001-6169-530X

335   J.S. Filhol: 0000-0002-3681-9267

336   H. Guesmi: 0000-0002-9369-523X

337   N. Romero: 0000-0002-2704-7779

338   P.Y. Blanchard: 0000-0003-1659-6868

339   J. Drnec: 0000-0002-9520-1555

340   J. Rozière: 0000-0001-6211-5047

341   D. Jones: 0000-0003-3787-2462

342   S. Cavaliere: 0000-0003-0939-108X

343

344   **Author Contributions**

345   The manuscript was written through contributions of all authors. All authors have given approval

346   to the final version of the manuscript.

347   **Author Contributions**

Carlos A. Campos-Roldán : Conceptualization, writing-original draft, formal analysis, investigation, **Raphaël Chattot** : Conceptualization, writing-review & editing, formal analysis, investigation, **Jean-Sébastien Filhol** : Writing-review & editing, formal analysis, methodology, **Hazar Guesmi** : Writing-review & editing, formal analysis, methodology, **Nuria Romero** : Methodology, investigation, writing-review & editing, **Rémi Bacabe** : Investigation, **Pierre-Yves Blanchard** : Writing-review & editing, supervision, **Valentin Vinci** : Writing-review & editing, investigation, **Jakub Drnec** : Writing-review & editing, formal analysis, investigation, **Jacques Rozière:** Funding acquisition, conceptualization, writing-original draft, supervision, **Deborah J. Jones** : Funding acquisition, conceptualization, writing-original draft, supervision, **Sara Cavaliere** : Funding acquisition, conceptualization, writing-original draft, supervision.

ASSOCIATED CONTENT

The following files are available free of charge.

Supporting Information: Comparison of the current state-of-the-art, experimental methodology, computational details, *ex situ* complementary characterization, complementary HAADF-STEM analyses after the electrochemical activation and after the AST, and *online* ICP-MS dissolution profile during the first AST 1,000 cycles are available in the Supporting Information.

ACKNOWLEDGEMENTS

REFERENCES

1.   van der Spek, M.; Banet, C.; Bauer, C.; Gabrielli, P.; Goldthorpe, W.; Mazzotti, M.; Munkejord, S. T.; Røkke, N. A.; Shah, N.; Sunny, N.; Sutter, D.; Trusler, J. M.; Gazzani, M., Perspective on the hydrogen economy as a pathway to reach net-zero CO_2 emissions in Europe. *Energy Environ. Sci.* **2022,** *15* (3), 1034-1077.

2.   Kodama, K.; Nagai, T.; Kuwaki, A.; Jinnouchi, R.; Morimoto, Y., Challenges in applying highly active Pt-based nanostructured catalysts for oxygen reduction reactions to fuel cell vehicles. *Nat Nanotechnol* **2021,** *16* (2), 140-147.

3.   Jiao, K.; Xuan, J.; Du, Q.; Bao, Z.; Xie, B.; Wang, B.; Zhao, Y.; Fan, L.; Wang, H.; Hou, Z.; Huo, S.; Brandon, N. P.; Yin, Y.; Guiver, M. D., Designing the next generation of proton-exchange membrane fuel cells. *Nature* **2021,** *595* (7867), 361-369.

4.   Ahn, C. Y.; Park, J. E.; Kim, S.; Kim, O. H.; Hwang, W.; Her, M.; Kang, S. Y.; Park, S.; Kwon, O. J.; Park, H. S.; Cho, Y. H.; Sung, Y. E., Differences in the Electrochemical Performance of Pt-Based Catalysts Used for Polymer Electrolyte Membrane Fuel Cells in Liquid Half- and Full-Cells. *Chem Rev* **2021,** *121* (24), 15075-15140.

5.   Zhao, L.; Zhu, J.; Zheng, Y.; Xiao, M.; Gao, R.; Zhang, Z.; Wen, G.; Dou, H.; Deng, Y. P.; Yu, A.; Wang, Z.; Chen, Z., Materials Engineering toward Durable Electrocatalysts for Proton Exchange Membrane Fuel Cells. *Adv. Energy Mater.* **2021,** *12* (2), 2102665.

6.   Borup, R. L.; Kusoglu, A.; Neyerlin, K. C.; Mukundan, R.; Ahluwalia, R. K.; Cullen, D. A.; More, K. L.; Weber, A. Z.; Myers, D. J., Recent developments in catalyst-related PEM fuel cell durability. *Curr Opin Electrochem* **2020,** *21*, 192-200.

7.   Campos-Roldán, C. A.; Pailloux, F.; Blanchard, P.-Y.; Jones, D. J.; Rozière, J.; Cavaliere, S., Rational Design of Carbon-Supported Platinum–Gadolinium Nanoalloys for Oxygen Reduction Reaction. *ACS Catal.* **2021,** *11* (21), 13519-13529.

8.   Greeley, J.; Stephens, I. E.; Bondarenko, A. S.; Johansson, T. P.; Hansen, H. A.; Jaramillo, T. F.; Rossmeisl, J.; Chorkendorff, I.; Norskov, J. K., Alloys of platinum and early transition metals as oxygen reduction electrocatalysts. *Nat Chem* **2009,** *1* (7), 552-6.

9.   Johannesson, G. H., Bligaard, T., Ruban, A., Skriver, H. L., Jacobsen, K. W., Nørskov, J. K., Combined electronic structure and evolutionary search approach to materials design. *Physical Review Letters* **2002,** *88* (25), 255506-255511.
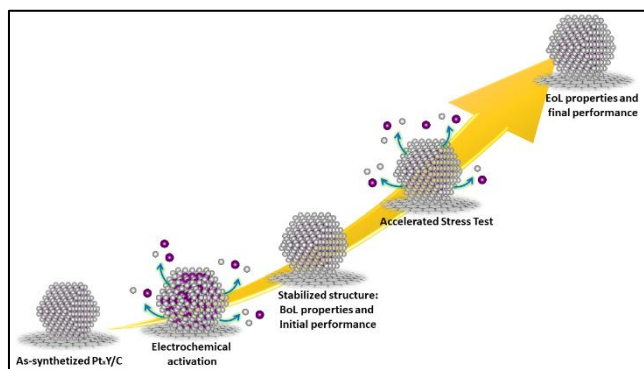
408 10. Stephens, I. E. L.; Bondarenko, A. S.; Bech, L.; Chorkendorff, I., Oxygen
409 Electroreduction Activity and X-Ray Photoelectron Spectroscopy of Platinum and Early
410 Transition Metal Alloys. *ChemCatChem* **2012,** *4* (3), 341-349.

411 11. Lindahl, N.; Zamburlini, E.; Feng, L.; Grönbeck, H.; Escudero-Escribano, M.;
412 Stephens, I. E. L.; Chorkendorff, I.; Langhammer, C.; Wickman, B., High Specific and Mass
413 Activity for the Oxygen Reduction Reaction for Thin Film Catalysts of Sputtered Pt_3Y. *Adv*
414 *Mater Interfaces* **2017,** *4* (13), 1700311.

415 12. Hernandez-Fernandez, P.; Masini, F.; McCarthy, D. N.; Strebel, C. E.; Friebel, D.;
416 Deiana, D.; Malacrida, P.; Nierhoff, A.; Bodin, A.; Wise, A. M.; Nielsen, J. H.; Hansen, T.
417 W.; Nilsson, A.; Stephens, I. E.; Chorkendorff, I., Mass-selected nanoparticles of Pt_xY as model
418 catalysts for oxygen electroreduction. *Nat Chem* **2014,** *6* (8), 732-8.

419 13. Pedersen, A. F.; Ulrikkeholm, E. T.; Escudero-Escribano, M.; Johansson, T. P.;
420 Malacrida, P.; Pedersen, C. M.; Hansen, M. H.; Jensen, K. D.; Rossmeisl, J.; Friebel, D.;
421 Nilsson, A.; Chorkendorff, I.; Stephens, I. E. L., Probing the nanoscale structure of the
422 catalytically active overlayer on Pt alloys with rare earths. *Nano Energy* **2016,** *29*, 249-260.

423 14. Hu, Y.; Jensen, J. O.; Cleemann, L. N.; Brandes, B. A.; Li, Q., Synthesis of Pt-Rare
424 Earth Metal Nanoalloys. *J Am Chem Soc* **2020,** *142* (2), 953-961.

425 15. Roy, C., Knudsen, B., Pedersen, C., Velazquez-Palenzuela, A., Christensen, L.,
426 Damsgaard, C., Stephens, I., Chorkendorff, I., Scalable Synthesis of Carbon-Supported
427 Platinum−Lanthanide and −Rare-Earth Alloys for Oxygen Reduction. *ACS Catal.* **2018,** *8*,
428 2071−2080.

429 16. Campos- Roldán, C. A.; Jones, D. J.; Rozière, J.; Cavaliere, S., Platinum- Rare Earth
430 Alloy Electrocatalysts for the Oxygen Reduction Reaction: A Brief Overview. *ChemCatChem*
431 **2022,** *14* (19), e202200334.

432 17. Brandiele, R.; Durante, C.; Grądzka, E.; Rizzi, G. A.; Zheng, J.; Badocco, D.;
433 Centomo, P.; Pastore, P.; Granozzi, G.; Gennaro, A., One step forward to a scalable synthesis of
434 platinum–yttrium alloy nanoparticles on mesoporous carbon for the oxygen reduction reaction. *J.*
435 *Mater. Chem. A* **2016,** *4* (31), 12232-12240.

436 18. Peera, S, Gwan Leea, T., Kumar Sahu, A., Pt-rare earth metal alloy/metal oxide catalysts
437 for oxygen reduction and alcohol oxidation reactions: an overview. *Sustainable Energy Fuels*
438 **2019,** *3*, 1866-1891.

439 19. Brandiele, R.; Guadagnini, A.; Girardi, L.; Dražić, G.; Dalconi, M.; Rizzi, G.;
440 Amendola, V.; Durante, C., Climbing the oxygen reduction reaction volcano plot with laser
441 ablation synthesis of Pt_xY nanoalloys. *Catal. Sci. Technol.* **2020,** *10* (14), 4503-4508.

442 20. Schwämmlein, J. N.; Harzer, G. S.; Pfändner, P.; Blankenship, A.; El-Sayed, H. A.;
443 Gasteiger, H. A., Activity and Stability of Carbon Supported Pt_xY Alloys for the ORR
444 Determined by RDE and Single-Cell PEMFC Measurements. *J Electrochem Soc* **2018,** *165* (15),
445 J3173-J3185.

446 21. Campos-Roldán, C. A.; Parnière, A.; Donzel, N.; Pailloux, F.; Blanchard, P.-Y.;
447 Jones, D. J.; Rozière, J.; Cavaliere, S., Influence of the Carbon Support on the Properties of
448 Platinum–Yttrium Nanoalloys for the Oxygen Reduction Reaction. *ACS Applied Energy*
449 *Materials* **2022,** *5* (3), 3319-3328.

450 22. Magnussen, O. M.; Drnec, J.; Qiu, C.; Martens, I.; Huang, J. J.; Chattot, R.; Singer,
451 A., In Situ and Operando X-ray Scattering Methods in Electrochemistry and Electrocatalysis.
452 *Chemical Reviews* **2024,** *124* (3), 629-721.

453 23.   Timoshenko, J.; Roldan Cuenya, B., In Situ/Operando Electrocatalyst Characterization by
454 X-ray Absorption Spectroscopy. *Chem Rev* **2021**, *121* (2), 882-961.
455 24.   Topalov, A. A.; Cherevko, S.; Zeradjanin, A. R.; Meier, J. C.; Katsounaros, I.;
456 Mayrhofer, K. J. J., Towards a comprehensive understanding of platinum dissolution in acidic
457 media. *Chem. Sci.* **2014**, *5* (2), 631-638.
458 25.   Malacrida, P.; Casalongue, H. G.; Masini, F.; Kaya, S.; Hernandez-Fernandez, P.;
459 Deiana, D.; Ogasawara, H.; Stephens, I. E.; Nilsson, A.; Chorkendorff, I., Direct observation of
460 the dealloying process of a platinum-yttrium nanoparticle fuel cell cathode and its oxygenated
461 species during the oxygen reduction reaction. *Phys Chem Chem Phys* **2015**, *17* (42), 28121-8.
462 26.   Campos-Roldan, C. A.; Pailloux, F.; Blanchard, P. Y.; Jones, D. J.; Roziere, J.;
463 Cavaliere, S., Enhancing the activity and stability of carbon-supported platinum-gadolinium
464 nanoalloys towards the oxygen reduction reaction. *Nanoscale Adv* **2021**, *4* (1), 26-29.
465 27.   Stariha, S.; Macauley, N.; Sneed, B. T.; Langlois, D.; More, K. L.; Mukundan, R.;
466 Borup, R. L., Recent Advances in Catalyst Accelerated Stress Tests for Polymer Electrolyte
467 Membrane Fuel Cells. *J. Electrochem. Soc.* **2018**, *165* (7), F492-F501.
468 28.   Campos-Roldán, C. A.; Chattot, R.; Filhol, J.-S.; Guesmi, H.; Pailloux, F.; Bacabe, R.;
469 Blanchard, P.-Y.; Zitolo, A.; Drnec, J.; Jones, D. J.; Cavaliere, S., Structure Dynamics of
470 Carbon-Supported Platinum-Neodymium Nanoalloys during the Oxygen Reduction Reaction.
471 *ACS Catalysis* **2023**, *13* (11), 7417-7427.
472 29.   Campos-Roldán, C. A.; Filhol, J.-S.; Guesmi, H.; Bigot, M.; Chattot, R.; Zitolo, A.;
473 Blanchard, P.-Y.; Rozière, J.; Jones, D. J.; Cavaliere, S., Stabilization of Carbon-Supported
474 Platinum–Rare Earth Nanoalloys during Electrochemical Activation. *ACS Catalysis* **2023**, *13*
475 (20), 13319-13324.
476 30.   Danisman, B.; Zhang, G. R.; Baumunk, A. F.; Yang, J.; Brummel, O.; Darge, P.;
477 Mayrhofer, K. J. J.; Libuda, J.; Ledendecker, M.; Etzold, B. J. M., Strong Activity Changes
478 Observable during the First Pretreatment Cycles of Trimetallic PtNiMo/C Catalysts.
479 *ChemElectroChem* **2023**, *10* (16), e202300109.
480 31.   Chattot, R.; Roiron, C.; Kumar, K.; Martin, V.; Campos Roldan, C. A.; Mirolo, M.;
481 Martens, I.; Castanheira, L.; Viola, A.; Bacabe, R.; Cavaliere, S.; Blanchard, P.-Y.; Dubau,
482 L.; Maillard, F.; Drnec, J., Break-In Bad: On the Conditioning of Fuel Cell Nanoalloy Catalysts.
483 *ACS Catalysis* **2022**, *12* (24), 15675-15685.
484 32.   Chattot, R.; Mirolo, M.; Martens, I.; Kumar, K.; Martin, V.; Gasmi, A.; Dubau, L.;
485 Maillard, F.; Castanheira, L.; Drnec, J., Beware of cyclic voltammetry! Measurement artefact in
486 accelerated stress test of fuel cell cathode revealed by operando X-ray diffraction. *Journal of
487 Power Sources* **2023**, *555*, 232345.
488 33.   Dukic, T.; Pavko, L.; Jovanovic, P.; Maselj, N.; Gatalo, M.; Hodnik, N., Stability
489 challenges of carbon-supported Pt-nanoalloys as fuel cell oxygen reduction reaction
490 electrocatalysts. *Chem Commun (Camb)* **2022**, *58* (100), 13832-13854.
491 34.   Sandbeck, D. J. S.; Inaba, M.; Quinson, J.; Bucher, J.; Zana, A.; Arenz, M.; Cherevko,
492 S., Particle Size Effect on Platinum Dissolution: Practical Considerations for Fuel Cells. *ACS
493 Appl Mater Interfaces* **2020**, *12* (23), 25718-25727.
494 35.   Gatalo, M.; Jovanovič, P.; Petek, U.; Šala, M.; Šelih, V. S.; Ruiz-Zepeda, F.; Bele,
495 M.; Hodnik, N.; Gaberšček, M., Comparison of Pt–Cu/C with Benchmark Pt–Co/C: Metal
496 Dissolution and Their Surface Interactions. *ACS Applied Energy Materials* **2019**, *2* (5), 3131-
497 3141.

498 36.   Fuchs, T., Drnec, J., Calle-Vallejo, F., Stubb, N., Sandbeck, D., Ruge, M., Cherevko, S.,
499 Harrington, D., Magnussen, O., Structure dependency of the atomic-scale mechanisms of
500 platinum electro-oxidation and dissolution. *Nat Catal* **2020,** *3*, 754-761.
501 37.   Dukic, T.; Moriau, L. J.; Pavko, L.; Kostelec, M.; Prokop, M.; Ruiz-Zepeda, F.; Sala,
502 M.; Drazic, G.; Gatalo, M.; Hodnik, N., Understanding the Crucial Significance of the
503 Temperature and Potential Window on the Stability of Carbon Supported Pt-Alloy Nanoparticles
504 as Oxygen Reduction Reaction Electrocatalysts. *ACS Catal* **2022,** *12* (1), 101-115.
505 38.   Sarwar, M.; Gavartin, J. L.; Martinez Bonastre, A.; Garcia Lopez, S.; Thompsett, D.;
506 Ball, S. C.; Krzystala, A.; Goldbeck, G.; French, S. A., Exploring fuel cell cathode materials
507 using ab initio high throughput calculations and validation using carbon supported Pt alloy
508 catalysts. *Phys Chem Chem Phys* **2020,** *22* (10), 5902-5914.
509 39.   Gan, L.; Heggen, M.; O'Malley, R.; Theobald, B.; Strasser, P., Understanding and
510 controlling nanoporosity formation for improving the stability of bimetallic fuel cell catalysts.
511 *Nano Lett* **2013,** *13* (3), 1131-8.
512 40.   Cho, J.; Kim, H.; Oh, H. S.; Choi, C. H., Elucidation of Electrochemically Induced but
513 Chemically Driven Pt Dissolution. *JACS Au* **2023,** *3* (1), 105-112.
514 41.   Duan, Z.; Henkelman, G., Atomic-Scale Mechanisms of Electrochemical Pt Dissolution.
515 *ACS Catalysis* **2021,** *11* (23), 14439-14447.
516 42.   Čolić, V.; Bandarenka, A. S., Pt Alloy Electrocatalysts for the Oxygen Reduction
517 Reaction: From Model Surfaces to Nanostructured Systems. *ACS Catal.* **2016,** *6* (8), 5378-5385.
518

519 **TOC graphic**

520